Atomistic simulations of radiation-induced defect formation in spinels: $MgAl_2O_4$, $MgGa_2O_4$, and $MgIn_2O_4$

D. Bacorisen and Roger Smith
Department of Mathematical Sciences, Loughborough University, Loughborough, Leicestershire LE11 3TU, United Kingdom

B. P. Uberuaga and K. E. Sickafus
Los Alamos National Laboratory, Los Alamos, New Mexico 87545, USA

J. A. Ball and R. W. Grimes
Department of Materials, Imperial College, Prince Consort Road, London SW7 2BP, United Kingdom
(Received 16 August 2006; revised manuscript received 17 October 2006; published 6 December 2006)

Molecular dynamics simulations of collision cascades were performed in three spinel oxides with varying inversion, namely normal magnesium aluminate, $MgAl_2O_4$, half-inverse magnesium gallate, $MgGa_2O_4$, and inverse magnesium indate, $MgIn_2O_4$. The response of each of these oxides for energies of up to 10 keV for the initial knock-on event was analyzed and compared. Defect production was characterized mainly by split interstitials/crowdions and cation antisite or disorder defects. The results show that cation interstitials preferentially occupy octahedral sites in all three materials. In the normal spinel, subcascade branching occurs and the defects at the end of the cascade are generally isolated, whereas in the half-inverse spinel, the higher energy cascades show a core damage region some of which consists of a partial rearrangement of atoms to the normal spinel structure and a partial transformation to a disordered rocksalt structure. In the fully inverse spinel a more connected region of the disordered rocksalt structure with the cascade core is evident.

DOI: 10.1103/PhysRevB.74.214105 PACS number(s): 61.72.Ji, 61.80.−x, 61.82.Ms

I. INTRODUCTION

There are many minerals in the Earth's mantle that take the form of the spinel structure. Some of those materials have been proposed as either nuclear waste forms or inert matrices for nuclear fuels. Thus an understanding of how they are affected by radiation is of fundamental scientific importance. Because of this, the impact of energetic particles on the microstructure of magnesium aluminate spinel, $MgAl_2O_4$, has been extensively studied by various experimental techniques to assess its radiation tolerance. These found that under neutron bombardment, its microstructure remained relatively stable, resulting in disordering replacements on the cation sublattice rather than point defect accumulation.[1] Disordering but no amorphization occurred when the material was irradiated with 1.5 MeV Kr^+ ions at 20 K to a high dose of 1×10^{16} ions/cm^2, while the same study revealed that if the sample was preirradiated by 400 and 50 keV Ne to introduce stable defects, followed by 1.5 MeV Kr^+ ions, partial amorphization could be seen.[2] However, the material underwent a phase transition to the disordered rocksalt structure under 180 keV Ne^+ ion irradiation at 120 K (Ref. 3) but showed signs of amorphization by 400 keV Xe^{2+} ion irradiation at 100 K.[4]

Based on these experimental observations, the relative strength of spinel to resist amorphization is primarily attributed to a high vacancy-interstitial recombination rate and to the ability of Mg and Al ions to swap lattice sites thereby sustaining the crystalline structure. These experimental investigations have also been supported by investigations using computational modeling.[5,6] However, Yu *et al.* suggested that the accumulation of cation disordering was the driving force to amorphization through an intermediate metastable crystalline phase.[4] Therefore it is important to understand how the presence of cation disorder might affect the radiation tolerance of the material. In other words, how radiation tolerant is a normal spinel as compared to a spinel with an inherent amount of cation disorder.

In this work we perform atomistic simulations to look at defect formation in normal magnesium aluminate, $MgAl_2O_4$, half-inverse magnesium gallate, $MgGa_2O_4$, and fully inverse magnesium indate, $MgIn_2O_4$, spinels using molecular dynamics (MD) simulations. $MgGa_2O_4$ and $MgIn_2O_4$ have similar crystalline structures to the normal $MgAl_2O_4$ but with different cation arrangements. Preliminary results of 0.4 and 2 keV cascades in these materials can be found in Ref. 6. This work supplements that presented in Ref. 6 by providing further analysis about the damage created in these three spinels at energies of up to 10 keV. The results presented here were obtained from a larger set of simulations.

During irradiation by high energy particles, atomic displacements occur over the time scale of picoseconds within

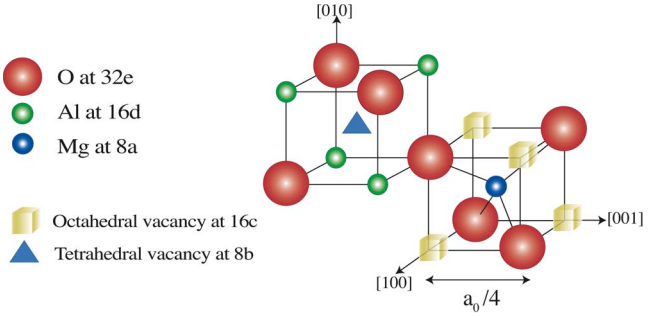

FIG. 1. (Color online) Diagram showing part of the unit cell of normal magnesium aluminate spinel with lattice parameter a_0.

TABLE I. Calculated bulk properties of the three spinels. a_0 denotes the lattice parameter, i, the inversion parameter, E_L and V are the lattice energy and volume per spinel molecule, and K denotes the bulk modulus.

Spinel	a_0 (Å)	i	E_L (eV/molecule)	V (Å/molecule)	K (GPa)
$MgAl_2O_4$	8.12 (8.14[a], 8.08[b])	0.0 (0.07[b])	−201.79 (−200.51[a])	66.97 (67.52[a])	272 (196[c])
$MgGa_2O_4$	8.31 (8.28[b])	0.5 (0.67[b])	−196.57	71.73	374
$MgIn_2O_4$	8.85 (8.81[b])	1.0 (1.0[b])	−181.81	86.64	238

[a]Reference 12: Chen *et al.* using the Bush *et al.* potential.
[b]Reference 13: Hill *et al.* (experiment).
[c]Reference 14: Kruger *et al.* (experiment).

the target material through elastic collisions and produce lattice defects which then diffuse more slowly. We model the process of defect production in spinels using MD simulations where an energetic projectile is fired into the crystal, disrupting its perfect ordering through collisions with lattice atoms. This sequence of atomic collisions is treated as being purely ballistic with no effect on the electronic state of the system. The nature and morphology of the damage created in the three spinels after several tens of picoseconds are investigated.

Spinels in general are oxides with the formula AB_2O_4, where A and B are either divalent and trivalent cations, respectively, or tetravalent and divalent.[7] One unit cell of spinel contains eight AB_2O_4 units arranged in an almost-perfect cubic closed-packed array of anions that contains tetrahedral and octahedral sites with $Fd3m$ space group symmetry. In a normal structure, one-eighth of the 64 tetrahedral sites are occupied by A^{2+} ions and half of the 32 octahedral interstices are taken up by B^{3+} ions. The positions of the ions with respect to the origin on an A-site cation using Wyckoff notation can be described as A at 8a, B at 16d, and O at 32e while the structural vacancies are located at 16c (octahedral site) and 8b and 48f (tetrahedral sites).[8] These structural vacancies may play an important role in defect process by accommodating interstitial species. For example, the spinel structure can be transformed to a rocksaltlike structure when the tetrahedrally coordinated cations move to octahedral interstices. Spinels can also exhibit cation mixing characterized by the inversion parameter i, the fraction of tetrahedral sites occupied by trivalent cations. Spinel compounds with $i=0$ are called normal spinels whereas those with $i=1$ are referred to as inverse spinels. In this work, the inversion parameters are assumed to be 0 for $MgAl_2O_4$ (normal spinel), 0.5 for $MgGa_2O_4$ (half-inverse spinel), and 1 for $MgIn_2O_4$ (inverse spinel), values that are close to the cation distributions in real materials.[9,10] The energetics of the three oxides under irradiation would therefore be attributed to the corresponding disorder as well as chemical effects of having different ternary cations (either Al^{3+}, Ga^{3+}, or In^{3+}) but all possess the same spinel structure. Figure 1 shows part of the structure of a normal spinel with Mg and Al ions occupying fourfold and sixfold coordinated sites, respectively, while the O^{2-} ions have 3 Al^{3+} and 1 Mg^{2+} as nearest neighbors.

II. METHODOLOGY

The calculations were based on a fixed charge model with a pairwise potential energy function, $\phi(r_{ij})$, comprised of the standard Buckingham potential and the usual electrostatics potential, $V(r_{ij})$, as shown by Eq. (1). Here r_{ij} refers to the distance between the interacting ions i and j.

$$\phi(r_{ij}) = A_{ij}\exp\left(-\frac{r_{ij}}{\rho_{ij}}\right) - \frac{C_{ij}}{r_{ij}^6} + V(r_{ij}). \tag{1}$$

The highly repulsive interactions arising from the ballistic phase of the collision cascades require splining of the poten-

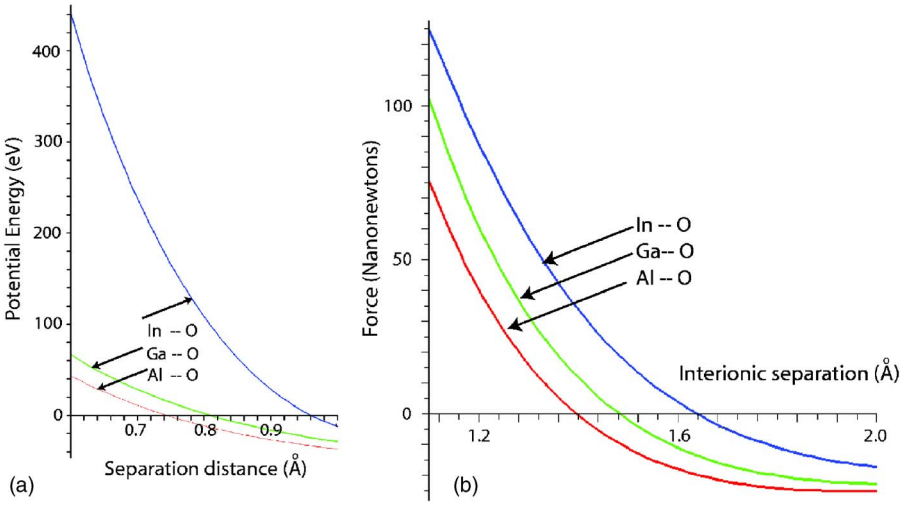

FIG. 2. (Color online) (a) The repulsive part of the pair interaction potential, including the Buckingham terms, the Coulombic terms, and the ZBL spline for the B-O interaction in the range 0.6–1.0 Å. (b) The pair interaction forces of the potentials near the equilibrium separation.

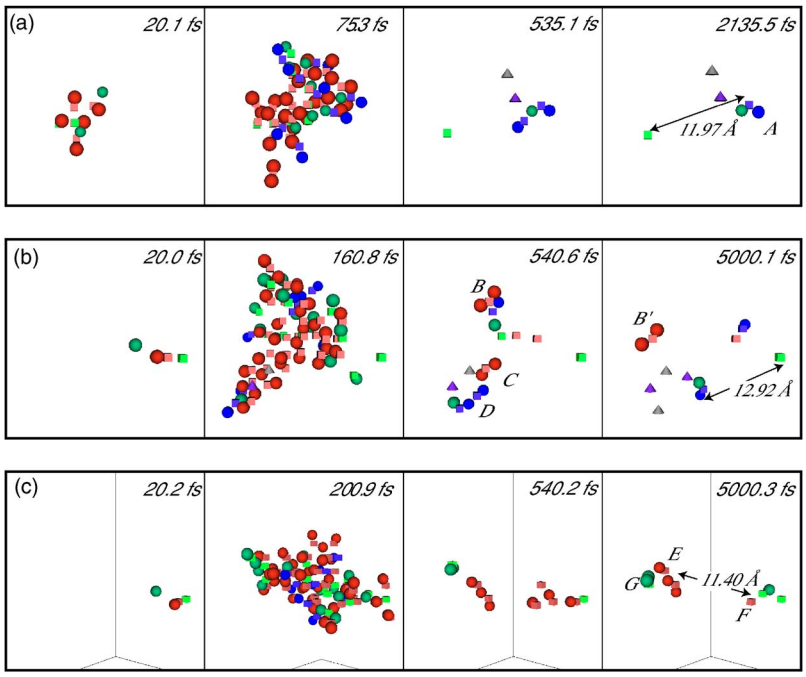

FIG. 3. (Color online) Snapshots of a 0.4 keV cascade simulation initiated by an Al (a), Ga (b), and In (c) PKA along ⟨123⟩ in the respective spinels. Only defects are shown. Spheres represent interstitials and cubes denote vacancies. The red color refers to O^{2-} defects, blue is for Mg^{2+} defects, while B^{3+} defects are colored green. Cation mixing is illustrated as purple and gray cones for Mg'_B and B'_{Mg} defects, respectively (B=Al, Ga, or In). The peak damage occurred approximately 75, 161, and 201 fs after the cascade was initiated in $MgAl_2O_4$, $MgGa_2O_4$, and $MgIn_2O_4$, respectively. Although no antisites/cation disorder defects occurred in (c), these defects were often observed at 0.4 keV.

tial energy function to the Ziegler-Biersack-Littmark (ZBL) potential.[11] Details for the potential parameters A_{ij}, ρ_{ij}, and C_{ij} are provided in Ref. 6. The lattice parameters resulting from our model are in good agreement with experimental data in all three spinels as shown in Table I. The lattice energy and volume per molecule of magnesium aluminate spinel show good agreement with those predicted by the Bush *et al.* potential which includes shell polarizability.[15] The bulk modulus in $MgAl_2O_4$ is overvalued by about 39% as compared to experimental data. This is because the structural properties of the materials were used during the fitting procedure and not their elastic properties. The vacancy migration energies reproduced by the $MgAl_2O_4$ potential are 1.67, 0.68, and 2.00 eV for the oxygen, magnesium, and aluminum vacancies, respectively,[16] and are in good agreement with the only known experimental value of 2.0±0.7 eV.[17] The repulsive parts of the trivalent cation (B)-O pair potentials are shown in Fig. 2. It can be clearly seen from this curve that the indate has a much steeper repulsion that the gallate which is also steeper than the normal spinel.

For the half-inverse and fully inverse spinels, $2\times1\times1$ unit cells containing 112 atom and representative of the appropriate inversion were generated by a combined Monte Carlo and energy minimization technique.[18] A number of possible cation distributions was generated for both the gallate and indate spinels at the required inversion of 0.5 and 1, respectively. The lattice energies of the various $2\times1\times1$ distributions were compared and the one with the lowest energy selected. For the MD simulations, larger cells were generated by replicating this unit cell along the three coordinate directions.

The simulations were performed in each of the $MgAl_2O_4$, $MgGa_2O_4$, and $MgIn_2O_4$ spinels separately using the parallel LBOMD code developed at Loughborough University. The energetic recoil was modeled by supplying extra kinetic energy to the principle knock-on atom (PKA) along a certain crystallographic direction and the cascade evolution was followed using the velocity Verlet integration algorithm with a variable time step. Cubic cells containing 12 331, 97 669, 450 461, and 988 391 particles were used for the different PKA energies of 0.4, 2, 5, and 10 keV, respectively. We performed a total of 27 simulations at the low energy of 0.4 keV, 24 simulations at energies of 2 and 5 keV, and a set of eight simulations for the 10 keV cascades in each oxide making a grand total of 249 simulations. In order to ensure that each individual cascade was unique and also that the results were statistically distributed for a given energy, different PKA directions, representative of a range of solid angles, as well as different species (Mg^{2+}, O^{2-}, or B^{3+} where B=Al, Ga, or In) were selected. Each trajectory was initiated at a temperature of 0 K and was followed up to 15 ps. For computational convenience, periodic boundary conditions were not employed, but instead a charge neutral simulation cell with three layers of fixed boundary atoms surrounding the active region was used. The Coulombic part of the calculation was evaluated using the distributed parallel multipole tree algorithm (DPMTA) which is a fast multipole method.[19]

III. DAMAGE RESULTING FROM CASCADE SIMULATIONS

In this work a displaced atom is referred to as an interstitial if it is further from a normal lattice site by $(\sqrt{3}/16)a_0$ Å, where a_0 denotes the lattice parameter of the spinel. This distance is half the separation between a tetrahedral cation and a nearest structural octahedral vacancy. It is still counted as an interstitial if it occupies a structural vacancy which is not a normal lattice site. Vacancies are similarly defined as original lattice sites with no atom within a radius of $(\sqrt{3}/16)a_0$ Å. The Kröger-Vink notation[20] is employed to describe the various defect species encountered. A split inter-

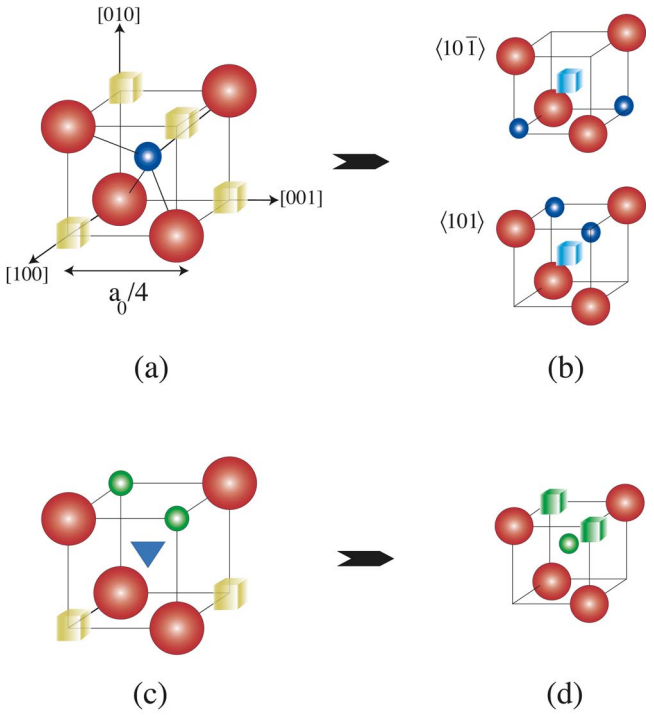

FIG. 4. (Color online) The perfect structure and defects in normal magnesium aluminate spinel: (a) shows a tetrahedrally coordinated Mg (blue sphere) with its 4 O nearest neighbors (red spheres) and four structural octahedral vacancies (yellow cubes). (b) An incoming Mg interstitial can knock out the tetrahedral Mg atom creating a split interstitial defect with the two interstitials now occupying octahedral sites and aligned along ⟨110⟩. (c) The inverted triangle denotes a 48*f* tetrahedral vacancy and the green spheres represent Al atoms in the perfect spinel structure. (d) A split vacancy defect consisting of two Al vacancies (green cubes) and one Al interstitial trapped at the tetrahedral site. This defect is often seen near an O vacancy.

stitial refers to two interstitials sharing a common vacancy, whereas a crowdion defect represents three interstitials occupying two vacancies. Longer interstitial-vacancy-interstitial chains are referred to as crowdion chains. In the normal spinel we refer to an antisite defect as an Mg ion on an Al site or vice versa. In the inverse and half-inverse spinels we refer to a change of cation species between the initial and final lattice arrangements as a cation disorder defect because their initial structures already contain disorder. However, an antisite defect in the fully inverse $MgIn_2O_4$ crystal refers to a Mg ion sitting at a tetrahedral In site.

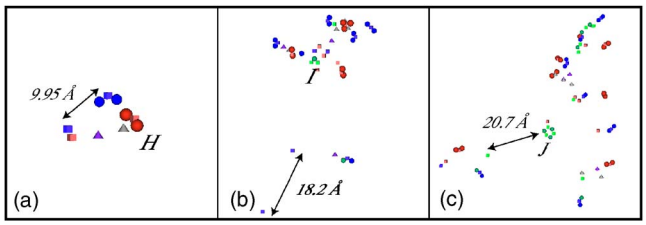

FIG. 5. (Color online) Spatial distribution of point defects in magnesium aluminate spinel: (a) 0.4 keV Mg PKA along ⟨1 7 11⟩, (b) 2 keV Mg PKA along ⟨210⟩, and (c) 5 keV Mg PKA in the ⟨157⟩ direction.

A. Postthreshold energy cascades

Figure 3 depicts snapshots for a typical 0.4 keV cascade in each spinel. Such low energy cascades are of interest because they have been shown to generate defects similar to those observed at higher energies.[21] Only the resulting defects are shown in the images. The cascade morphology during the collisional phase is very similar in the three compounds at this energy and most of the defects annihilate within the first picosecond. Figure 4 shows how some of the most commonly observed cation interstitial and vacancy defects in normal spinel are arranged. This is similar to the defect distribution in the other two spinels at that energy.

The residual damage in magnesium aluminate shown in Fig. 3(a) consists of 1 Al vacancy (V'''_{Al}), a pair of cation antisite defects (Mg'_{Al} and $Al^{\cdot}_{Mg}$), and a cation split interstitial centered about a tetrahedral Mg vacancy labeled *A*. The split interstitial has the following arrangement: two of the four empty octahedral sites (at 16*c*) around the central tetrahedral Mg vacancy (8*a* site) hold the two interstitials in a ⟨110⟩ alignment. This defect is not linear, but subtends an angle with the central vacancy as shown in Fig. 4(b), effectively filling two of the empty corners of a cubic cell. If the other two corners of this cell were to be similarly filled this would produce a local structure with the rocksalt arrangement of ions. The split interstitial can also include an Al and Mg ion rather than two Mg ions but split interstitials involving two Al ions were never observed. Similarly, isolated Al interstitials were not seen in the cascades and were found to be unstable.[16]

Figure 3(b) illustrates the damage evolution in the half-inverse Ga spinel. After 541 fs, anion split interstitials defects labeled *B* and *C* were seen to move one-dimensionally along ⟨110⟩ directions. The defect *C* recombines with a $V^{\cdot\cdot}_{O}$, initially 7.6 Å away, whereas defect *B* remains in the structure becoming *B'* after 5 ps. The movement of cations on the cation sublattice is illustrated by the cation defect chain labeled *D*, consisting of three alternate interstitials and two vacancies, which relaxed to form two cation disorder defects and 1 $Mg^{\cdot\cdot}_{i}$-V''_{Mg}-$Ga^{\cdot\cdot\cdot}_{i}$. In the spinel structure, split interstitials are observed to be centered about a tetrahedral vacancy (8*a* site).[5] These sites are equally occupied by both Ga and Mg ions in the half-inverse spinel, where the cation split interstitials were observed to be centered about.

A typical cascade evolution and the surviving defects in magnesium indate are shown in Fig. 3(c). The anion interstitials relaxed into a crowdion defect labeled *E*, which oscillated one-dimensionally along ⟨110⟩ at the end of the collisional phase of the cascade. The anion vacancy, *F*, created some local distortion pushing the first nearest neighbor tetrahedral In ion off its perfect lattice position. In analogy to the normal $MgAl_2O_4$ spinel where cation split interstitials were centered about a tetrahedral Mg vacancy, crowdions in the inverse spinel were also centered about the tetrahedral cation vacancy, with the interstitials occupying the neighboring structural octahedral vacancies [an example is the defect *G* in Fig. 3(c)].

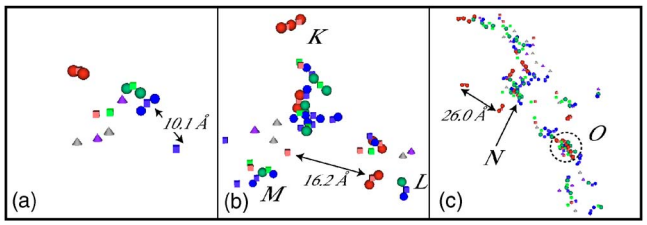

FIG. 6. (Color online) Residual defects at the end of 0.4, 2, and 5 keV cascades for a Mg PKA set along ⟨123⟩, ⟨789⟩, and ⟨512⟩ direction, respectively, in the Ga spinel.

B. 2–10 keV cascades

The low-energy 0.4 keV cascades showed how cation interstitials form relatively stable split interstitials during the collisional phase of the cascade. These could also diffuse locally on the cation sublattice and annihilate completely or form stable antisites/cation disorder defects over longer times. During the cascade relaxation in all three spinels, the anion split interstitials or crowdion structures move only on the anion sublattice before settling down as the energy in the cascade was dissipated. These defects were also seen in the higher energy cascades and have relatively low energy barriers for motion, at least locally. By increasing the PKA energy, more defects were created and the cascades became more complex in the half-inverse and inverse spinels as compared to the normal spinel. Figures 5–7 show the damage caused by Mg PKAs with knock-on energies of 0.4, 2, and 5 keV in all three spinels. Figures 8 and 9 compare typical cascades in the three spinels for 5 and 10 keV PKAs and Fig. 10 analyzes the disorder in the cascade core for the 5 keV PKAs. The 10 keV cascades in all three spinels were initiated only by cation PKAs because of long range channelling when choosing an oxygen PKA. It was not possible to contain an anion PKA cascade even using a lattice of 3 million atoms.

1. $MgAl_2O_4$ *normal spinel*

In the normal magnesium aluminate spinel, the same typical defect structures were seen for 0.4, 2, 5, and 10 keV PKAs consisting of split interstitials centered about a tetrahedral Mg vacancy and anion split interstitials along the ⟨110⟩ array of anions. The effects of subcascade branching resulted in well-defined and separate defects even for 10 keV

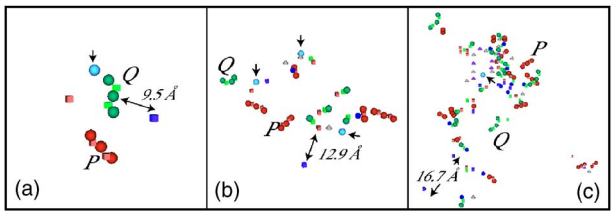

FIG. 7. (Color online) Defects at the end of 0.4, 2, and 5 keV cascades for a Mg PKA set along ⟨173⟩, ⟨135⟩, and ⟨123⟩ direction, respectively, in the fully inverse In spinel. The bright blue spheres, indicated by the arrows, denote Mg ions occupying tetrahedral sites, Mg_{In}^{T}, while the cones represent cation disordering on the octahedral sublattice.

PKAs as shown in Fig. 9(a). Recombination of O_i''-$V_O^{\cdot\cdot}$-O_i'' split interstitials with $V_O^{\cdot\cdot}$ could occur via a one-dimensional interstitialcy mechanism along ⟨110⟩ with occasional reorientation to other ⟨110⟩ axes. The one-dimensional (1D) diffusion mechanism has an energy barrier of 0.29 eV while the rotation mechanism has an activation energy of 0.64 and 0.67 eV.[16] However, this motion could be pinned by the presence of a nearby $Al_{Mg}^{\cdot}$ defect. Such a situation is marked *H* in Fig. 5(a). The higher energy cascades spread over a larger volume of the simulation cell as can be seen by comparing Figs. 5(b) and 5(c), Figs. 8(a)–8(c), and Fig. 9(a). Some interesting defect structures were observed on the Al^{3+} sublattice labeled *I* [Al split vacancy as in Fig. 4(d)] and *J* (Al "ring" consisting of three alternate Al ions and vacancies) in Fig. 5, whereby the interstitials were trapped at tetrahedral sites between the actual vacancies. The Al ring structure has a formation energy of 10.2 eV. This is much larger than the formation energy of antisite pairs but less than the vacancy-split interstitial Frenkel pairs.[5] As a result of the displacement cascades on the cation sublattice, cation interstitials could occupy octahedral sites when forming split interstitials while the formation of split vacancy and ring defects on the Al sublattice caused interstitials to occupy tetrahedral sites. Ring defects with one or two Mg interstitials were also occasionally observed but more prevalent were isolated vacancies, cation-anion vacancy pairs, and antisites, the Al vacancy often occurring paired with an anion vacancy. A few cation crowdion defects were also observed at the higher energies—an example of a $Mg_i^{\cdot\cdot}$-V_{Mg}''-$Al_i^{\cdot\cdot\cdot}$-V_{Mg}''-$Mg_i^{\cdot\cdot}$ is evident in region (2) of Fig. 9(a). During the recrystallization phase at the end of the cascade there was very little motion observed on the Al sublattice. Most Al interstitials either settled to Mg antisites with the displaced Mg ion moving on the Mg sublattice or formed split interstitials with an Mg ion as shown in Fig. 4(b).

2. $MgGa_2O_4$ *half-inverse spinel*

The damage imparted to the anion sublattice in the half-inverse gallate spinel consisted of both split interstitials and crowdions, an example of which is shown labeled *K* in Fig. 6(b). Cation interstitials could form split interstitials, crowdions, and even crowdion chains, labeled *L*, *M*, and *N* in Fig. 6. These can sometimes relax to an antisite and a split interstitial as seen in Fig. 3(b). The damage morphology shown in Figs. 6(b) and 6(c) indicate much more local disordering than in the normal spinel where the defects are more isolated. Moreover, the damage in region O [Fig. 6(c)] is interesting because it contains one oxygen antisite defect, O_{Ga}, which under normal circumstances, would be an energetically unfavorable defect. In this case, the anion antisite defect is surrounded by 3 Ga interstitials which partially balance the charge. Defect production by 10 keV cascades in $MgGa_2O_4$ was characterized by more cation interstitial-vacancy networks sometimes forming closed loops as shown in region (4) of Fig. 9(b) where cations are displaced from their initial sites to adjacent structural vacancy sites in the crystal. As seen also in the 2 and 5 keV cascades, cation interstitials could occupy both octahedral and tetrahedral sites in these crowdion chains.

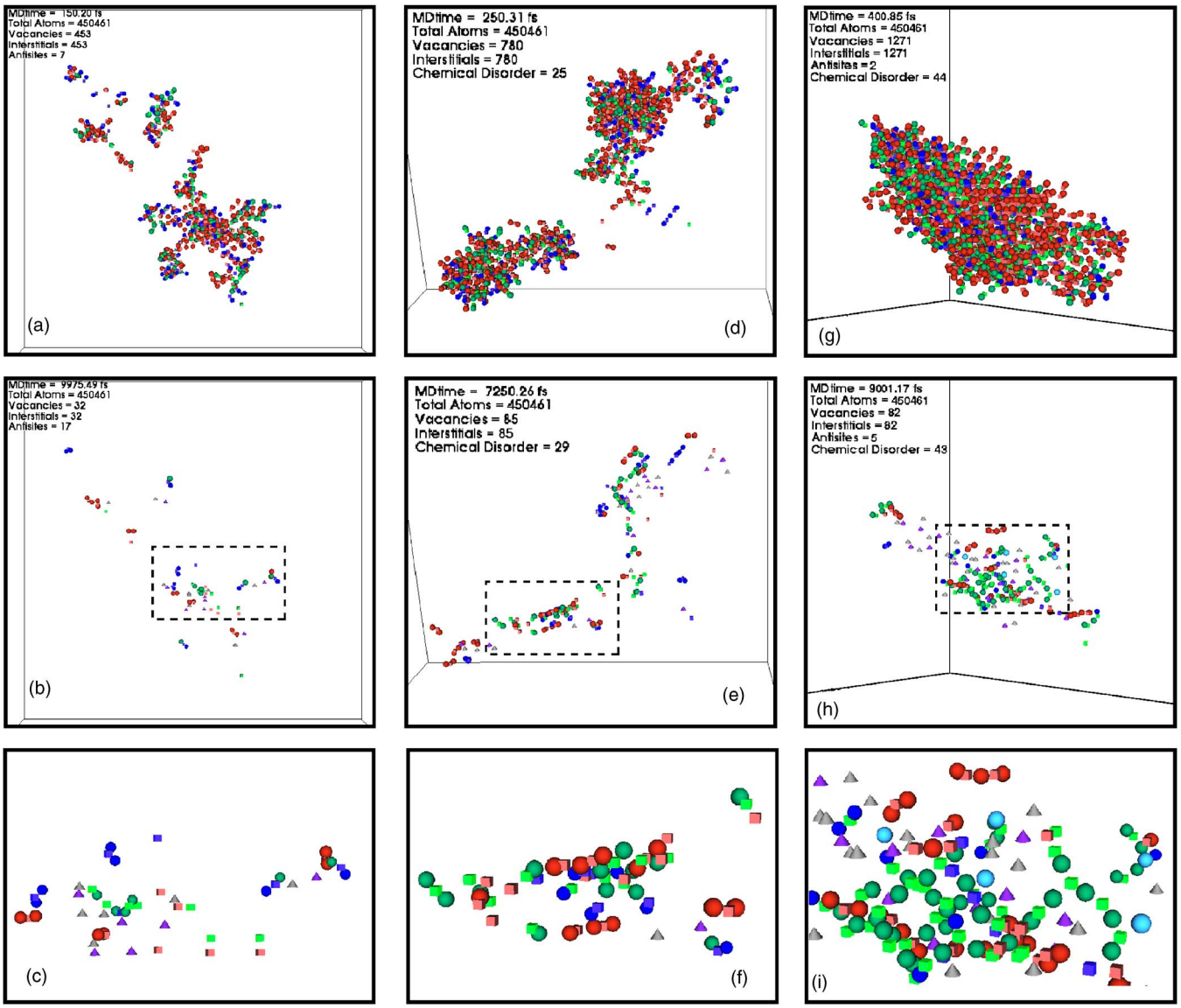

FIG. 8. (Color online) Cascades generated by a 5 keV PKA in the three spinels showing the displacement of ions when there is peak damage and also at the end of the collisional phase of the cascade. (a) 150 fs, (b) and (c) 9975 fs, normal $MgAl_2O_4$ spinel and Al PKA; (d) 250 fs, (e) and (f) 7250 fs, half-inverse $MgGa_2O_4$ spinel and Ga PKA; (g) 400 fs, (h) and (i) 9001 fs, fully inverse spinel, $MgIn_2O_4$ and In PKA. (c), (f) and (i) are zoom-ins of the core of the cascades.

3. $MgIn_2O_4$ *inverse spinel*

Radiation damage in the fully inverse spinel was characterized by the formation of more anion and In crowdions consisting of three interstitials at octahedral interstices and two vacancies. These defects are illustrated in Fig. 7 labeled *P*, and *Q*, respectively. Along certain PKA directions, networks of cation interstitials and vacancies could be identified in the core of the cascade and were even more predominant than in the half-inverse spinel [see Fig. 8(i)]. The chains were mainly created on the In^{3+} sublattice in the fully inverse spinel whereas in the half-inverse spinel, these involved both the octahedral and tetrahedral sublattices. Oxygen vacancies could also cause a greater displacement of the nearby tetrahedral In ions than in the other two materials. There are three cases of this evident in Fig. 7(b). Due to the full inversion of the $MgIn_2O_4$ spinel, no Mg ions occupied tetrahedral sites initially, but these could be generated during the cascades and formed Mg'_{In} antisites. There were some differences in the cascade morphology for the 10 keV PKAs between the In and Mg PKAs in the inverse $MgIn_2O_4$ crystal. Mg PKAs resulted in more subcascade branching and defect spreading as in the normal spinel whereas In PKAs produced dense cascade cores which took longer to recrystallize. However, the types of defects were similar to those seen at the 2 and 5 keV energies irrespective of the PKA type. Figure 9(c) shows some of these defects with distinctive In chains, oxygen crowdions, and cation disorder defects.

4. *Analysis of the cascade cores for the three spinels*

The crystalline ordering around the cation interstitials reveal distinct characteristics in each of the three spinels. Se-

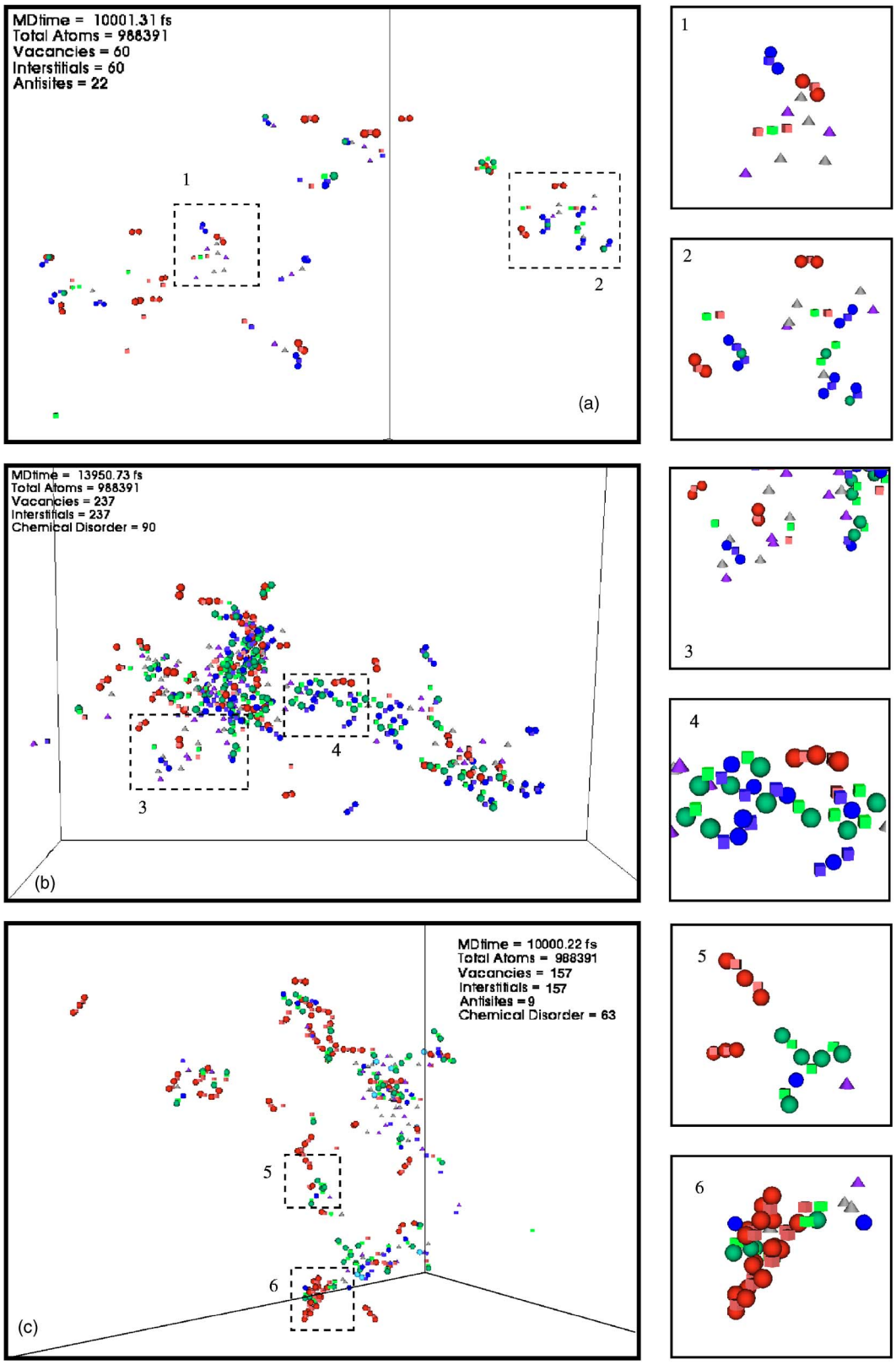

FIG. 9. (Color online) Defects remaining at the end of the collisional phase of a 10 keV cascade in (a) $MgAl_2O_4$ initiated by an Al PKA along ⟨8 13 7⟩; (b) $MgGa_2O_4$ and Ga PKA along the ⟨132⟩ trajectory that caused the most damage over a set of eight simulations; (c) $MgIn_2O_4$ and In PKA along ⟨235⟩ resulting in the most defects over a set of eight simulations. The length of the cubic simulation cells was approximately 23 nm.

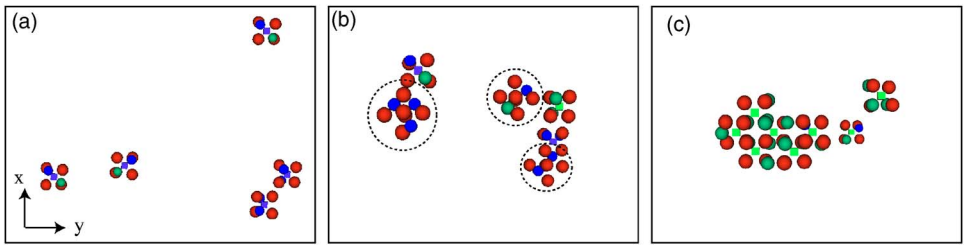

FIG. 10. (Color online) Differences in the crystalline ordering around cation interstitials taken from regions of the 5 keV cascades in Fig. 8. The red spheres denote oxygen atoms at perfect sites, blue spheres refer to Mg interstitials, green spheres denote B interstitials (B=Al, Ga, or In), and the cubes denote cation vacancies. (a) The cation split interstitials in $MgAl_2O_4$ are similar to those obtained at the low 0.4 keV cascades and are arranged as shown in Fig. 4(b). (b) The regions encircled denote cation interstitials having tetrahedral coordination in the half-inverse $MgGa_2O_4$ spinel. (c) The green cubes denote tetrahedral vacancies in the inverse $MgIn_2O_4$ spinel—around each tetrahedral vacancy, three cation interstitials fill up three of the four empty 16c octahedral interstices.

lected regions of interest around cation interstitials are taken from the 5 keV cascades in Fig. 8 and are plotted with their nearest oxygen neighbors also shown in Fig. 10. In Fig. 10(a) for the normal spinel, typical cation split interstitials aligned along ⟨110⟩ are obtained similar to those illustrated in Fig. 4(b). The same types of defects were seen in the half-inverse spinel, but these are connected to regions whereby cation interstitials move to tetrahedral sites [see encircled regions in Fig. 10(b)], reforming locally the spinel structure but offset from the original half-inverse system. Figure 10(c) depicts regions in the inverse spinel where the cascade has caused a depletion of cations from their tetrahedral sites. The interesting feature about these defects is that three of the four empty 16c octahedral sites around each vacancy are now occupied by cation interstitials. In the normal spinel, the split interstitials in Fig. 10(a) occupy only two of the four empty octahedral sites. This implies a slightly different and more complete postcascade disordered rocksalt structure transformation in the inverse spinel compared to the normal spinel.

The evolution of the number of interstitials with time for a 5 keV B^{3+} PKA (B=Al, Ga, or In) in the three materials is shown in Fig. 11. These show that the peak damage increases and occurs at longer times as the degree of inversion increases. The immediate postcascade annealing process also takes longer. The trends shown in these figures are typical of all cascades in these materials.

IV. POSTCASCADE DEFECT DISTRIBUTION IN THE SPINEL STRUCTURES

The graphs in Figs. 12(a)–12(c) indicate the average number and species of the interstitials (solid lines), vacancies (dashed lines), and cation disorder (CD) defects per simulation that remain in the three spinels at the corresponding energies. These results must be treated with some caution since they are dependent on the precise definition of what forms a defect. For example the crowdion is counted as three interstitial defects and two vacancies whereas the split interstitial is counted as two interstitials and one vacancy. Notwithstanding this proviso, from this plot, magnesium aluminate spinel produced the least number of point defects as compared to the half and fully inverse spinels. For the nor-

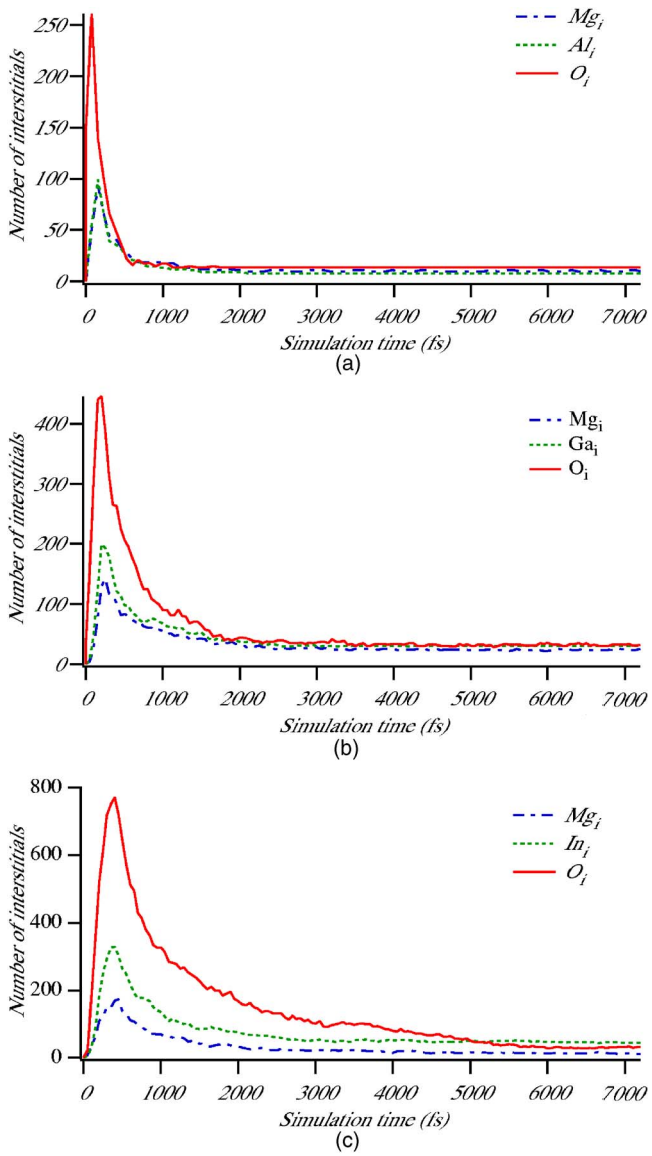

FIG. 11. (Color online) Comparison of the defect evolution (number of interstitials) with time in the corresponding 5 keV cascades shown in Fig. 8 in (i) $MgAl_2O_4$, (ii) $MgGa_2O_4$, and (iii) $MgIn_2O_4$.

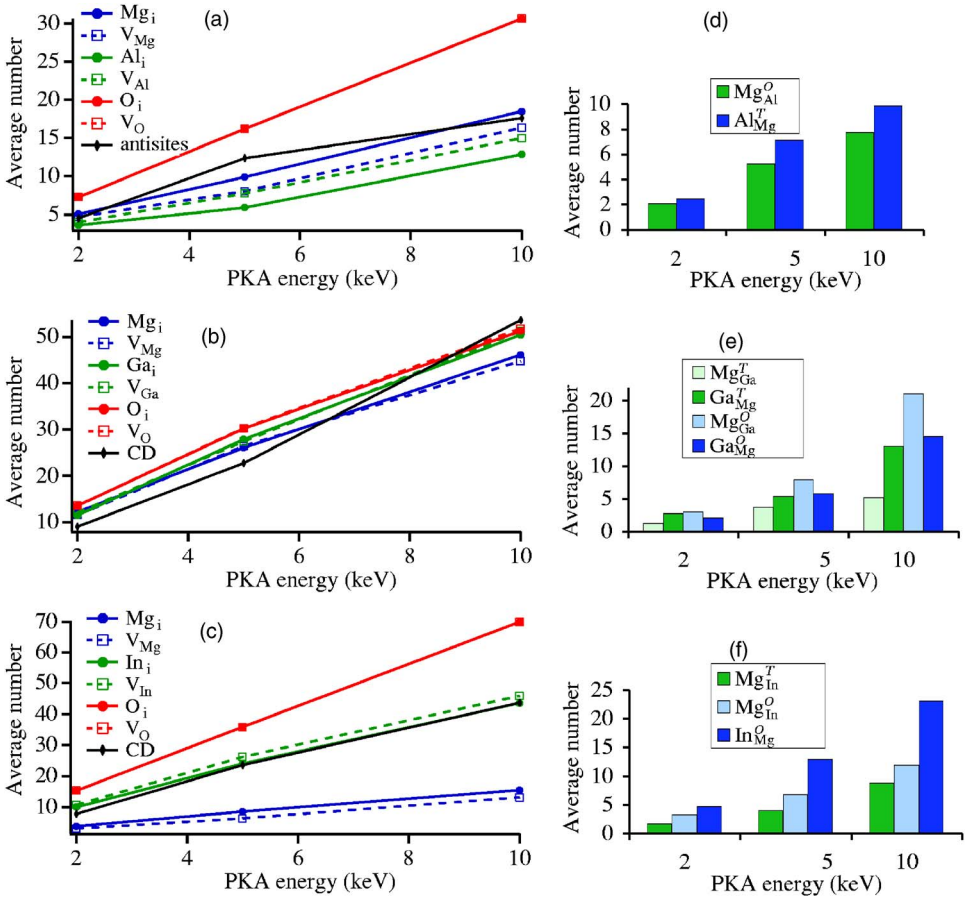

FIG. 12. (Color online) Average number of interstitials, vacancies, and antisites/cation disorder (CD) defects created per simulation at energies of 2, 5, and 10 keV in (a) normal spinel, $MgAl_2O_4$, (b) half-inverse $MgGa_2O_4$, and (c) inverse spinel. The average number and type of cation disorder defects and their coordination are shown in (d), (e), and (f). The superscripts *T* and *O* refer to tetrahedral and octahedral coordination, respectively.

mal and fully inverse spinels (as would be expected since there are more O ions) there are more displaced O ions than cations. There are slightly more displaced Mg ions than Al in normal spinel despite there being twice as many Al ions in the lattice than Mg. This situation is reversed in the fully inverse spinel due to the fact that in the first case tetrahedral sites are occupied by Mg^{2+} but in the second case these sites are filled by In^{3+}. It thus appears to be much easier to displace ions from tetrahedral sites than octahedral. Figures 12(a)–12(c) indicate differences in the number of cation interstitials and vacancies because of the formation of antisites/cation disorder defects in the spinels. The difference is most apparent in the normal spinel, showing that there are more Al vacancies than Al interstitials due to the formation of more Al_{Mg} antisites than Mg_{Al} antisites. The same plot in the half-inverse spinel reveals an almost identical number of cation vacancies and interstitials remaining in the irradiated structure and these are comparable with the number of anion defects and cation disorder defects. This is due to the fact that cations tend to be displaced from their lattice sites around O defects, not that more cations are formed by the ballistic displacement. In the normal and fully inverse spinels, the number of O interstitial defects is equal to the number of O vacancies (red curves in Fig. 12), but not in the half-inverse spinel because of the formation of a small number of anion antisites in the disordered cascade core. The highest number of anion defects was recorded in inverse spinel due to a preference for the formation of crowdion defects rather than split interstitials. The average number of total interstitial defects for the 10 keV cascades in $MgAl_2O_4$ was 62, 148 in $MgGa_2O_4$, and 129 in $MgIn_2O_4$, with standard deviations of 7, 40, and 16, respectively. This indicates a wider spread of damage range in the half-inverse spinel.

Cation disordering in all three compounds represents one of the major defects resulting from the dynamical cascades. These defects result from cations swapping from octahedrally to tetrahedrally coordinated sites or vice versa producing antisites in the normal spinel, but could also involve interchange of cations of different species over similar sites in the half-inverse and inverse spinels. The plots in Figs. 12(d)–12(f) show the average number of cation disorder defects per simulation distributed over tetrahedral and octahedral sites. In the normal spinel radiation creates antisites of the form Mg^O_{Al} and Al^T_{Mg}, where the superscripts *O* and *T* refer to the octahedral and tetrahedral sites. Figure 12(d) indicates a slightly higher number of Al antisites than Mg antisites created in the normal spinel at all three energies. This can be partly explained by the fact that during the cascade relaxation, the mixed split interstitial, $Mg_i^{\cdot\cdot}$-V''_{Mg}-$Al_i^{\cdot\cdot\cdot}$, could form an Al_{Mg} antisite and a pure $Mg_i^{\cdot\cdot}$-V''_{Mg}-$Mg_i^{\cdot\cdot}$ split interstitial which could then move locally on the tetrahedral Mg sublattice before stabilizing. In the half-inverse $MgGa_2O_4$ spinel, radiation causes a redistribution of cations as shown in Fig. 12(e). This indicates that the Ga_{Mg} cation disorder defects are equally distributed on both the tetrahedral and octahedral Mg sites whereas the Mg_{Ga} prefer octahedral coordination over tetrahedral coordination. This implies that the half-inverse spinel (initially with an inversion of 0.5) can

TABLE II. The percentage of cation interstitials occupying structural tetrahedral (*Tetra*) and octahedral (*Octa*) sites at the end of the collision cascades.

	2 keV		5 keV		10 keV	
Spinel	*Tetra*	*Octa*	*Tetra*	*Octa*	*Tetra*	*Octa*
$MgAl_2O_4$	23.9	74.2	21.6	74.2	19.9	76.9
$MgGa_2O_4$	38.2	46.8	34.9	52.8	33.2	55.6
$MgIn_2O_4$	17.7	62.2	17.6	66.5	17.4	67.2

become more inverse as a result of irradiation. In the inverse spinel, Mg_{In}^{T} antisite defects were seen, which were not present in the original lattice. This induces a partial reversion from the inverse to the normal spinel structure. However, the plot in Fig. 12(f) also shows more In_{Mg}^{O} and Mg_{In}^{O} cation disorder defects that remain in the structure than the antisites. These results show that every spinel accommodates a large amount of cation site interchange under irradiation which helps in maintaining the crystalline structure.

In order to investigate the preferential segregation of cation interstitials to certain sites, we filter out those interstitials that are trapped at structural vacancies and regain coordination four (tetrahedral site) or six (octahedral site) with the anions. The figures shown in Table II represent the distribution of cation interstitials at tetrahedral or octahedral structural vacancies for a given energy. It should be noted that the percentages do not add up exactly to 100% because not all the interstitials are located at those structural vacancies but can be trapped between other defects. A similar approach is employed to investigate the nature of the cation vacancies left over at the end of the cascades and is presented in Table III. This information reveals the extent by which the octahedral and tetrahedral sites are depleted of their cations under irradiation.

Table II shows a clear difference between the percentage of octahedral and tetrahedral interstitial site occupancies in the normal $MgAl_2O_4$ and inverse $MgIn_2O_4$ spinels with more octahedral sites being occupied at all three PKA energies. However, this is smallest for the intermediate $MgGa_2O_4$ spinel which has the highest tetrahedral site occupancies among the three spinels of 38.2%, 34.9%, and 33.2% for energies of 2, 5, and 10 keV, respectively. Nevertheless, in all three spinels, the cation interstitials preferentially move to octahedral sites rather than tetrahedral sites under irradiation.

TABLE III. The percentage of tetrahedral (*Tetra*) and octahedral (*Octa*) cation vacancies remaining at the end of the cascade simulations.

	2 keV		5 keV		10 keV	
Spinel	*Tetra*	*Octa*	*Tetra*	*Octa*	*Tetra*	*Octa*
$MgAl_2O_4$	54.1	45.9	50.9	49.1	52.2	47.8
$MgGa_2O_4$	44.4	55.6	48.4	51.6	48.4	51.6
$MgIn_2O_4$	65.5	34.5	67.8	32.2	65.3	34.7

The vacancy distribution shown in Table III indicates that in the normal spinel and in the semi-inverse gallate spinel, both the octahedral and tetrahedral cation sublattices are almost equally affected. However, in one unit cell of spinel, there are twice as many occupied cation octahedral sites (16) than tetrahedral sites (8)—one would expect more displaced octahedral ions (and hence more octahedral vacancies) than displaced tetrahedral ions—yet both sublattices are depleted by a similar amount. Therefore it ought to be easier to displace tetrahedrally coordinated ions than octahedrally coordinated ions. This observation was also recorded under neutron irradiation during which diffraction patterns in the irradiated sample were reduced by 20% for the tetrahedral sites but increased by 8% for the octahedral sites.[1] This is more evident in the inverse $MgIn_2O_4$ spinel where more tetrahedral vacancies than octahedral vacancies remain in the structure coupled with an increased octahedral site occupancy (see Table II), at all three energies investigated. Therefore the inverse spinel is more susceptible to undergo the rocksalt transformation as compared to the normal and half-inverse spinels.

V. DISCUSSIONS AND CONCLUSIONS

Molecular dynamics simulations were performed at PKA energies of 0.4–10 keV to investigate the effects of radiation in spinels with varying inversion. In all three spinels, the normal $MgAl_2O_4$, the half-inverse $MgGa_2O_4$, and the fully inverse $MgIn_2O_4$ spinel, the onset of damage production resulted in simple defect structures consisting of split interstitials/crowdions and cation disorder defects. Over the time scale of the collisional phase, a cation split interstitial could remain in the structure, diffuse on the tetrahedral sublattice to annihilate with a nearby vacancy in the structure, or form an immobile antisite/cation disorder defect. Oxygen split interstitials/crowdions were aligned along the ⟨110⟩ array of anions and could diffuse along that path with occasional orientation change to another ⟨110⟩ direction.

The higher energy cascades in normal spinel only produced distinct point defects characteristic of the low energy cascades due to subcascade branching. On the other hand, dense cascades in the half-inverse and fully inverse spinels created complex damage zones consisting of chains of interstitials and vacancies on the cation sublattice. In the half-inverse spinel, cation interstitials could occupy both tetrahedral and octahedral sites whereas cation defects in the inverse spinel were primarily In^{3+} defects. Cascades spread out more in the normal spinel compared to the inverse spinels and relaxation also occurred more quickly in the normal spinel.

The simulations showed that cation interstitials preferentially occupied octahedral sites irrespective of the spinel type. However, in the inverse spinel, the increased octahedral site occupancy was coupled with a depletion of ions on the tetrahedral In sublattice indicating a faster structural transformation under radiation than in the normal spinel, with the half-inverse $MgGa_2O_4$ spinel showing the least propensity for this transformation. In the latter case, regions of the crystal could recrystallize among the point defects by forming

cation chains of interstitials and vacancies with the interstitials residing at adjacent tetrahedral and octahedral vacancy sites.

The process of defect recombination in this particular group of spinels is dependent on at least three factors: first on the presence of cation disorder, second on the nature of the chemical bonding in the spinel, and third on the steepness of the repulsive wall between the trivalent cations and the O ions. Isolating these factors is not trivial. Based on structural considerations only, one would predict a better damage recovery in an isotropic crystal as compared to an anisotropic one. The random distribution of divalent and trivalent cations in the inverse spinels contributes to changes in bond lengths locally in the crystal resulting to some degree of anisotropy. This affects the damage recovery process as compared to the normal spinel which resulted in the least number of surviving defects at the end of the cascade simulations. The second factor is attributed to chemical effects arising from the increase in atomic number of the trivalent B^{3+} ions from Al^{3+} to Ga^{3+} to In^{3+}. It is known that the ability of a crystal structure to regain its crystalline ordering depends on the degree of ionicity or covalency of the material.[22] The hypothesis in Ref. 22 is that this is determined by the short-range term of the potential energy function. Here it was identified that different damage recovery can be obtained depending on the steepness of the O-O interaction near equilibrium.[23] In our simulations, the short range O-O pair interaction is the same for all three spinels, whereas the *B*-O interaction changes according to the trivalent cation. The repulsive walls for the *B*-O interactions are shown in Fig. 2 along with the forces near the equilibrium separation. The steepness of the potential curves is partially correlated with the remaining damage after the cascade in that the normal spinel, which has the least repulsive wall, shows the least damage. This is also a feature of cascades in metals where the resultant damage after the cascade is highly dependent on the steepness of this curve in the region 1–100 eV. The steepness ordering is also the same near equilibrium where the forces are plotted in Fig. 2(b). Thus there is also qualitative agreement with the hypothesis of Ref. 22 which associates damage recovery with this near-equilibrium steepness. However, it is difficult to quantify this as damage depends on so many other features of the model such as the initial degree of inversion, other parts of the potential interaction regime, the relative mass of the ions, and especially the barriers for defect recombination.

Over the time scales studied, two diffusion mechanisms have been depicted in the normal spinel (1D motion of the O split interstitial and the cation split interstitial moving on the tetrahedral sublattice). For the half-inverse and inverse spinels the crowdion/split interstitial defects oscillate locally but do not move long distances after the ballistic phase is over. These preliminary results seem to indicate that defect recombination is easier in the normal spinel structure. This is currently being investigated and the defect formation energies, diffusion paths, and energy barriers for transitions will be presented in subsequent publications.[16]

[1] K. E. Sickafus, A. C. Larson, N. Yu, M. Nastasi, G. W. Hollenberg, F. A. Garner, and R. C. Bradt, J. Nucl. Mater. **219**, 128 (1995).

[2] N. Bordes, L. M. Wang, R. C. Ewing, and K. E. Sickafus, J. Mater. Res. **10**, 981 (1995).

[3] M. Ishimaru, I. V. Afanasyev-Charkin, and K. E. Sickafus, Appl. Phys. Lett. **76**, 2556 (2000).

[4] N. Yu, K. E. Sickafus, and M. Nastasi, Philos. Mag. Lett. **70**, 235 (1994).

[5] R. Smith, D. Bacorisen, B. P. Uberuaga, K. E. Sickafus, J. A. Ball, and R. W. Grimes, J. Phys.: Condens. Matter **17**, 875 (2005).

[6] D. Bacorisen, R. Smith, J. A. Ball, R. W. Grimes, B. P. Uberuaga, K. E. Sickafus, and W. T. Rankin, Nucl. Instrum. Methods Phys. Res. B **250**, 36 (2006).

[7] A. N. Cormack, G. V. Lewis, S. C. Parker, and C. R. A. Catlow, J. Phys. Chem. Solids **49**, 53 (1988).

[8] K. E. Sickafus, J. M. Wills, and N. W. Grimes, J. Am. Ceram. Soc. **82**, 3279 (1999).

[9] J. E. Weidenborner, N. R. Stemple, and Y. Okaya, Acta Crystallogr. **20**, 761 (1966).

[10] J. B. Goodenough and A. L. Loeb, Phys. Rev. **98**, 391 (1955).

[11] J. P. Biersack, J. Ziegler, and U. Littmark, *The Stopping Range of Ions in Solids* (Pergamon Press, Oxford, 1985).

[12] S. P. Chen, M. Yan, J. D. Gale, R. W. Grimes, R. Devanathan, K. E. Sickafus, N. Yu, and M. Nastasi, Philos. Mag. Lett. **73**, 51 (1996).

[13] R. J. Hill, J. R. Craig, and G. V. Gibbs, Phys. Chem. Miner. **4**, 317 (1979).

[14] M. B. Kruger, J. H. Nguyen, W. Caldwell, and R. Jeanloz, Phys. Rev. B **56**, 1 (1997).

[15] T. S. Bush, J. D. Gale, C. R. A. Catlow, and P. D. Battle, J. Mater. Chem. **4**, 831 (1994).

[16] B. P. Uberuaga, D. Bacorisen, R. Smith, J. A. Ball, R. W. Grimes, A. F. Voter, and K. E. Sickafus, Phys. Rev. B (to be published).

[17] K. Yasuda, C. Kinoshita, K. Fukuda, and F. A. Garner, J. Nucl. Mater. **283**, 937 (2000).

[18] M. O. Zacate and R. W. Grimes, Philos. Mag. A **80**, 797 (2000).

[19] W. T. Rankin and J. A. Board, Jr., *Proceedings of the 1995 IEEE Symposium on High Performance Distributed Computing* (IEEE Computer Society Press, Los Alamitos, CA, 1995), p. 17.

[20] F. A. Kröger and H. A. Vink, *Solid State Physics: Advances in Research and Applications* (Academic, New York, 1957).

[21] B. P. Uberuaga, R. Smith, A. R. Cleave, F. Montalenti, G. Henkelman, R. W. Grimes, A. F. Voter, and K. E. Sickafus, Phys. Rev. Lett. **92**, 115505 (2004).

[22] K. Trachenko, J. M. Pruneda, E. Artacho, and M. T. Dove, Phys. Rev. B **71**, 184104 (2005).

[23] K. Trachenko, M. T. Dove, E. Artacho, I. T. Todorov, and W. Smith, Phys. Rev. B **73**, 174207 (2006).